doi:10.26443/seismica.v4i2.1702

The 09 December 2024 Mw5.7 Parker Butte Earthquake: Orthogonal surface fracturing and associated ground disturbances near Yerington, Nevada, central Walker Lane

Rich D. Koehler [*1], **Christie D. Rowe** [2], **Dominic R. Vlaha** [3], **Simone Masoch** [4], **Nicole Wagoner** [1,3], **Yu Jiang** [2], **Kyren Bogulub** [2], **Daniel Trugman** [2], **William C. Hammond** [4], **Aren Crandall-Bear** [4], **Christopher Kratt** [5], **Kayleigh Dohm** [3], **Jennifer Vlcan** [1]

[1]Nevada Bureau of Mines and Geology, University of Nevada, Reno, Reno, NV USA, [2]Nevada Seismological Laboratory, University of Nevada, Reno, Reno, NV USA, [3]Department of Geological Sciences and Engineering, University of Nevada, Reno, Reno, NV USA, [4]Nevada Geodetic Laboratory, Nevada Bureau of Mines and Geology, University of Nevada, Reno, Reno, NV USA, [5]Center for Transformative Environmental Sensing Programs, University of Nevada, Reno, Reno, NV USA

Author contributions: *Conceptualization*: R. Koehler, C. Rowe. *Methodology*: Koehler, Bogulub, Trugman, Jiang, Hammond, Crandall-Bear, Kratt, Dohm. *Formal Analysis*: R. Koehler, C. Rowe. *Investigation*: R. Koehler, C. Rowe, D. Vlaha, S. Masoch, N. Hart-Wagoner, C. Kratt, K. Dohm. *Analysis of seismic data*: K. Bogolub, D. Trugman. *Analysis of geodetic and Insar data*: Y. Jiang, A. Crandall-Bear, W. Hammond. *Public data dissemination and clearinghouse*: J. Vlcan. *Writing - Original draft*: R. Koehler, C. Rowe. *Writing - Review & Editing*: all authors. *Visualization*: R. Koehler, C. Rowe, K. Bogolub, Y. Jiang, D. Vlaha, C. Kratt, K. Dohm.

Abstract The Mw5.7 Parker Butte earthquake occurred on 09 December, 2024, ∼24 km NNE of Yerington (western Nevada, USA) due to sinistral slip on an unmapped ENE-striking fault. Field reconnaissance and a drone survey were conducted within <1-8 days and ∼1 month, respectively, after the earthquake. We observed a lack of surface rupture above the ENE-striking plane of the mainshock and most aftershocks, as well as surface fracturing along a NW-trending lineament orthogonal to the mainshock. Shaking effects included minor sediment failures, liquefaction features, and short-lived fracturing and refreezing features in ice on the Walker River and agricultural channels. Damage to infrastructure was minimal, only settlement and cracking of one bridge abutment fill prism. We estimate ground motions of up to 0.4 g and 23 cm/s. These observations provide valuable data about the effects of moderate magnitude earthquakes and highlight the importance of coordinated multidisciplinary geodetic, seismologic, and field geologic responses. The orthogonal faults indicated by the mainshock and the secondary surface fractures are part of a pattern in the region, where orthogonal faults have slipped in several historical earthquake sequences, establishing this as a common style of faulting within the complex network of faults that comprise the Walker Lane.

Non-technical summary This paper describes the effects of the Mw5.7 Parker Butte earthquake that occurred on 09 December 2024 northeast of Yerington, Nevada, based on rapid field reconnaissance of the epicentral area and analysis of seismic, geodetic, and InSAR data. The results indicate that the earthquake occurred on an ENE-striking fault that did not reach the surface but caused minor secondary shaking effects such as mass wasting and liquefaction, as well as minor NW-striking surface fracturing along a secondary fault. The study highlights the importance of documenting perishable geologic effects and improves the understanding of the effects of moderate earthquakes in the Walker Lane.

Production Editor: Gareth Funning
Handling Editor: Alexandra Hatem
Copy & Layout Editor: Hannah F. Mark

Received: April 21, 2025
Accepted: August 27, 2025
Published: October 15, 2025

1 Introduction

The Mw5.7 Parker Butte earthquake occurred on 09 December 2024 at 3:08 PM local time / 23:08 UTC, approximately 24 km NNE of Yerington, western Nevada and approximately 63 km east of the State's capital in Carson City (Figures 1 and 2a). In the days after the event, the U.S. Geological Survey recorded over 12,000 felt reports from as far away as San Francisco and Salt Lake City. The reports indicate that Modified Mercalli shaking intensities were strong in the epicentral area (MMI VI) and moderate in Reno and Carson City (MMI V). However, due to the event's remote location with little infrastructure and sparse population, no damage or notable societal impacts were reported.

Preliminary seismic data (moment tensor and aftershock pattern) indicate that the earthquake initiated at a depth of 9.3 km. Aftershocks were distributed along a northeast (060°)-striking zone extending ∼8 km across the northern Mason Valley between Parker Butte and the Desert Mountains with a left-lateral sense of motion (Figure 2b). The fault indicated by the mainshock and aftershocks was not previously mapped, but it is subparallel to the Wabuska Lineament (Figure 1), a Quaternary-active fault zone along the range front of the Desert Mountains (Li et al., 2017) approximately 6

*Corresponding author: rkoehler@unr.edu

km north of the epicenter. The last historical earthquake in this area was the poorly located 25 June 1933 >M6 Wabuska earthquake, speculated by some to have occurred along the westward projection of the Wabuska Lineament or along the Singatse Range fault (Slemmons et al., 1965; dePolo and dePolo, 2012; Li et al., 2017).

Field documentation of the effects of the earthquake commenced on 10 December 2024 and was led by a multidisciplinary team from the University of Nevada, Reno including members from the Nevada Bureau of Mines and Geology (NBMG), Nevada Seismological Laboratory (NSL), and the Department of Geological Sciences and Engineering (DGSE). Data collection included detailed observations on the presence or absence of surface rupture, the types and distribution of perishable secondary earthquake effects, and damage to infrastructure. The field reconnaissance consisted of driving unimproved roads (Julian Lane and several unimproved spur roads) along the Walker River floodplain as well as walking transects across the aftershock zone. Subsequent field reconnaissance was conducted on 12 and 14 December 2024 in the epicentral area, as well as 17 December 2024 with the aim of inspecting lineaments identified on Sentinel-1 InSAR interferograms calculated by the U.S. Geological Survey and the NSL on 16 December 2024 that suggested the presence of surface deformation. An Uncrewed Aircraft System (UAS) survey was conducted on 15 January 2025 along one of the InSAR lineaments, resulting in an orthophoto mosaic, digital surface model, and hillshade (Supplemental Section S1).

We report field observations made within 8 days after the earthquake. No evidence for surface rupture was observed along the NE-trending zone of aftershocks, where InSAR and GPS evidence revealed slip at depth related to the mainshock. A short (1.5 km-long) continuous surface fracture array in Campbell Valley was observed along a NW-trending lineament discovered in the InSAR data that roughly coincides with the diffuse NW-trending zone of aftershocks south of the main rupture (Figures 2b and 2c). Shaking-related secondary earthquake effects were documented in the epicentral area and particularly along the Walker River.

2 Regional context of the Parker Butte earthquake

The Parker Butte earthquake occurred in the central Walker Lane seismic belt (Figure 1) that extends along the eastern side of the Sierra Nevada and accommodates about 10–25% of the Pacific/North American plate boundary motion (Hammond and Thatcher, 2007). In this area, deformation is accommodated along N-striking normal faults, NW-striking right-lateral faults, and NE-striking left-lateral faults (Wesnousky, 2005). The geodetic velocity field indicates that NW-directed dextral shear of ∼8 mm/yr is distributed across the central Walker Lane at the latitude of the Parker Butte earthquake (Hammond et al., 2024).

The epicenter lies within a series of left-stepping, en echelon asymmetric basins that extend from Walker Lake to Lake Tahoe (Figure 1). The physiographic expression of the basins indicates that Quaternary deformation is primarily accommodated by N-striking, east-dipping normal faults that bound the basins. GPS block modeling suggests that a component of oblique or partitioned right-lateral fault slip is also needed to accommodate geodetically observed shear (Bormann et al., 2016). Pierce et al. (2021) determined vertical slip rates along faults bounding Smith and Mason valleys of 0.5 mm/yr and 0.04 mm/yr, respectively, and presented geomorphic evidence consistent with right-normal oblique slip on N- to NW-striking faults. Similarly, south of the Parker Butte earthquake, oblique slip has also been documented in paleoseismic studies along the Wassuk Range fault where late Pleistocene vertical and right-lateral slip rates have been determined to be 0.4-0.7 mm/yr (Bormann et al., 2012) and ∼1 mm/yr (Dong et al., 2014), respectively.

Active NE-striking left-lateral faults occur north of the epicenter including the Wabuska and Carson lineaments. These structures have been referred to as lineaments in the Walker Lane literature for decades (Stewart and Ernst, 1988), however they are clearly faults with evidence for Quaternary deformation including aligned tectonic geomorphic features (Li et al., 2017). Evidence for late Pleistocene displacement across the Wabuska Lineament includes scarps and laterally offset stream channels incised into alluvial fan deposits that have been used to estimate a maximum left-lateral slip rate of 0.7 mm/yr (Li et al., 2017). To the south, faults with similar NE orientations have generated historical earthquakes, including the 1934 M6.3 Excelsior Mountains (Callaghan and Gianella, 1935) and 2020 Mw6.5 Monte Cristo Range earthquakes (Koehler et al., 2021). South-southeast of the epicenter, well-expressed northwest-striking right-lateral strike-slip faults bound the eastern side of the central Walker Lane where the Benton Spring, Indian Head, Gumdrop, and Petrified Springs faults together accommodate ∼4 mm/yr of dextral shear (Angster et al., 2019).

Of the ∼8 mm/yr dextral shear strain suggested by geodetic studies in this region, geologic studies can attribute ∼5.4 mm/yr (∼68%) to mapped active faults (Dong et al., 2014; Angster et al., 2019; Pierce et al., 2021; Hammond et al., 2024). Additional dextral deformation is thought to be accommodated through oblique deformation on dip-slip faults, clockwise block rotations, distributed faulting within basins, slip on unknown dextral faults, and possibly coseismic warping (Cashman and Fontaine, 2000; Wesnousky et al., 2012; Pierce et al., 2021; Say and Zuza, 2021).

3 Observations

3.1 Event details from seismic and geodetic networks

The nearest permanent seismic station to the earthquake sequence is located ∼25 km away, west of Yerington (NN-YER; Figure 2a). In addition to the field reconnaissance, the NSL deployed five temporary seismometers in the vicinity of the epicenter to capture

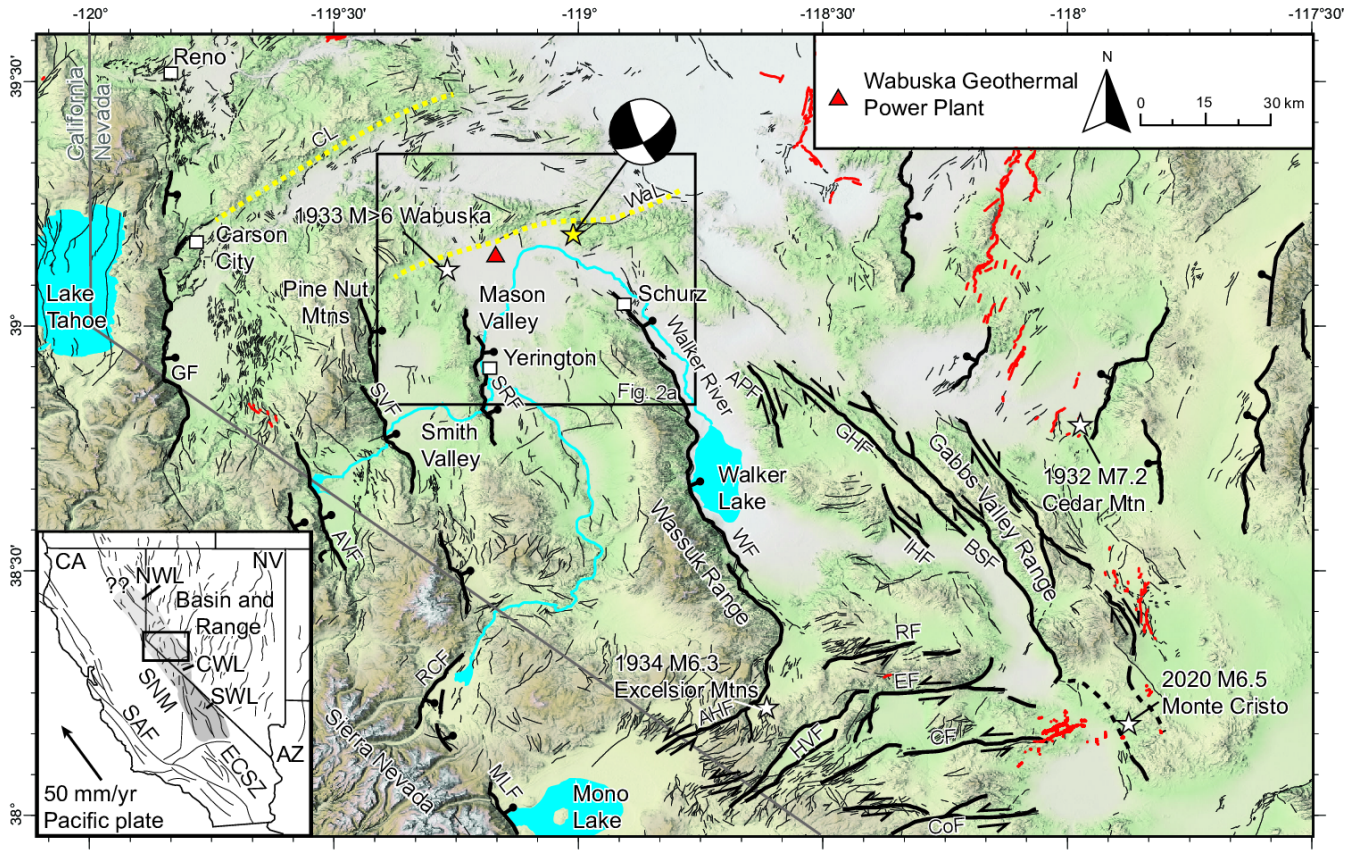

Figure 1 Regional map showing Quaternary faults of the central Walker Lane and epicenter of the Parker Butte earthquake (yellow star; coordinates: 39.168°N, 119.024°W). White stars are historic earthquakes. Major named faults (bold black lines) and other faults (thin black lines) from USGS Quaternary fault and fold database. Yellow dotted lines are named lineaments (Wal, Wabuska Lineament; CL, Carson Lineament) and red lines are historic surface ruptures. GF, Genoa fault; AVF, Antelope Valley fault; RCF, Robinson Creek fault; MLF, Mono Lake fault; SVF, Smith Valley fault; SRF, Singatse Range fault; WF, Wassuk Range fault; APF, Agai Pah fault; GHF, Gumdrop Hills fault; IHF, Indian Head fault; BSF, Benton Springs fault; RF, Rattlesnake fault; EF, Excelsior fault; CF, Candelaria fault; CoF, Coaldale fault; HVF, Huntoon Valley fault. Inset shows regional tectonic setting and extent of map (black box). NWL, northern Walker Lane; CWL, central Walker Lane; SWL, southern Walker Lane; ECSZ, Eastern California Shear Zone; SAF, San Andreas fault.

aftershocks (Figure 2a). Nearly 300 aftershocks were recorded in the first three days after the mainshock, including 20 aftershocks of magnitude > M3, mostly along the inferred rupture plane and also beneath the northern Wassuk Range extending south-southeast of the main rupture plane (detailed analysis in Bogolub et al., 2025) (Figure 2b).

The Nevada Geodetic Laboratory operates several continuously and semi-continuously recording GPS stations in the Mobile Array of GPS for Nevada Transtension network (MAGNET) near the epicenter; NSF EarthScope operates two continuous stations for the Geodetic Facility for the Advancement of Geoscience (GAGE), and the Northern Nevada Cooperative Real Time Network operates a station in Yerington (Figure 2a). Preliminary assessment of the geodetic signal indicated that stations on either side of the earthquake moved about 1 cm, with displacement azimuths consistent with left-lateral slip. The NBMG launched an event page on the Nevada Earthquake Clearinghouse (https://nevada-earthquake-clearinghouse-nbmg.hub.arcgis.com/pages/parker-butte-earthquake) to support field operations, inform local news outlets, and archive geospatial data and photographs of the field surveys.

3.2 Field reconnaissance observations

The observations of surface fractures and secondary shaking effects are the result of rapid reconnaissance of the earthquake and are not comprehensive. Although the observed geologic effects are typical of a moderate earthquake, we acknowledge that additional surface fracturing could have occurred in areas not examined and that minor secondary shaking effects are likely more widespread than we observed. The locations of field observations colored by type are shown on Figure 2c. All GPS coordinates reported herein are in the format of latitude and longitude, referenced to the WGS84 coordinate system.

3.3 Surface rupture/fracturing

We did not identify surficial displacements or ground cracking in the area of the NE-trending aftershock zone

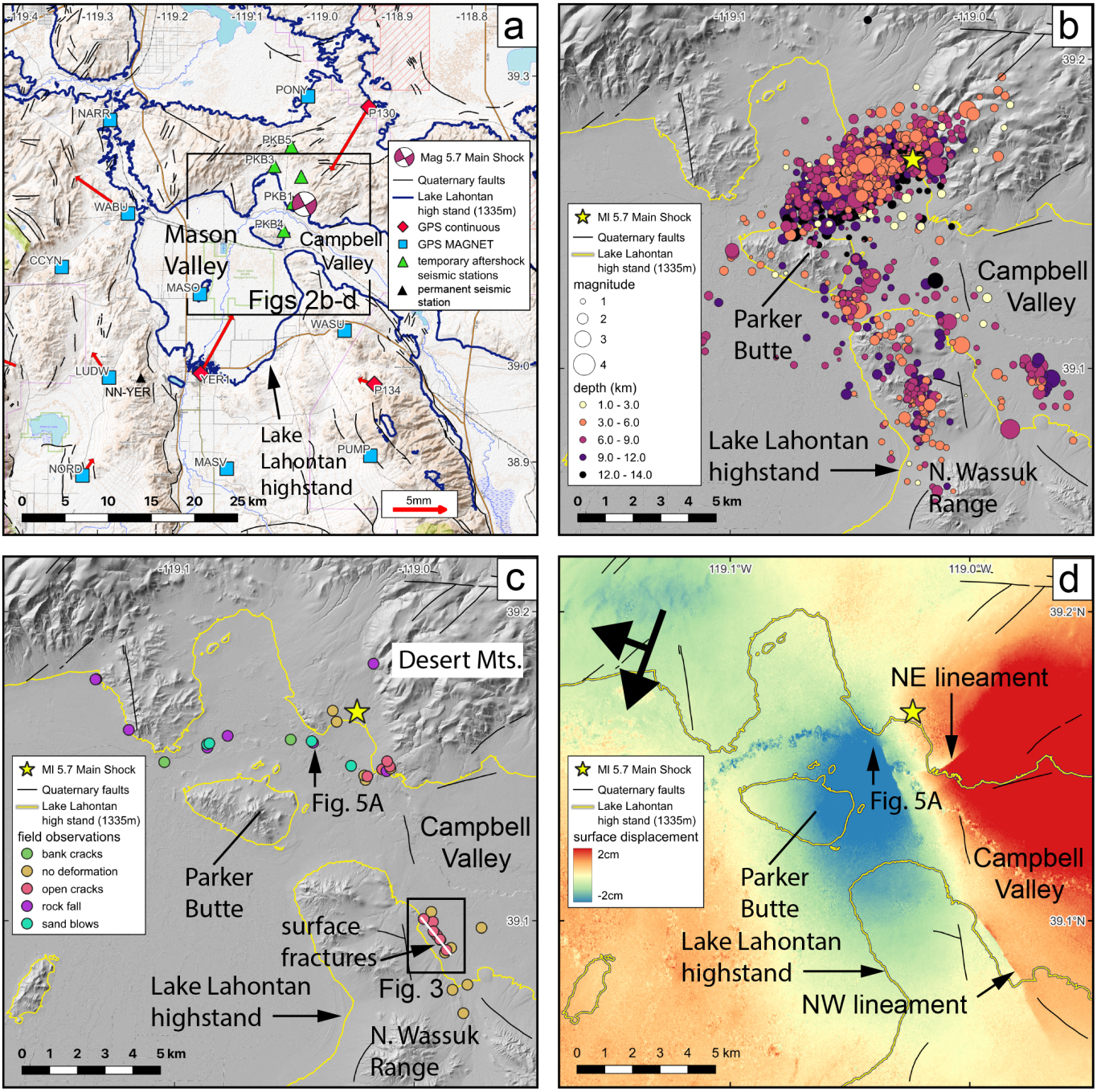

Figure 2 Maps of the epicentral area of the Parker Butte earthquake. (a) Region physiography and geography, temporary seismic stations (green triangles), GPS stations (blue squares, MAGNET; red diamonds, continuous), and relative crustal velocities (red arrows). (b) Lidar hillshade map showing the spatial distribution of aftershock seismicity color coded by depth. (c) Lidar hillshade map showing locations of field observations colored by type. White line indicates extent of surface fracture array. (d) Stacked unwrapped InSAR phase derived from four Sentinel-1 descending interferograms, 2024/11/03-2014/12/21, 2024/11/15-2014/12/21, 2024/11/27-2014/12/21, 2024/12/09-2014/12/21, processed by NSL. Locations of the NW- and NE-trending lineaments indicated. Bold black arrows are satellite flight (long) and look direction (short). Earthquake epicenter (yellow star and focal mechanism) and highstand elevation of pluvial Lake Lahontan indicated in all panels. Base map in (a) from opentopomap.org based on World Geodetic System 1984 ensemble (EPSG:6326). Bare earth lidar hillshades in panels (b) and (c) from US Geological Survey (2023), 1-m resolution.

(inferred mainshock plane) suggesting that the earthquake rupture did not reach the surface. There was a complete absence of aligned or recent surface cracks in the epicentral area, and no widespread crack arrays were observed in our field surveys made on the 10th, 12th, and 14th of December. Additionally, we observed no tectonic geomorphic features (i.e., scarps) in the field or in USGS 1m lidar crossing alluvial fans and lacustrine deposits along the aftershock zone between the Walker River and the epicenter, consistent with a long period of tectonic quiescence on the mainshock fault (Fig. 2b; discussed further in Section: Older Faulting).

Sentinal-1 InSAR interferograms of the epicentral area became available on 16 December (ascending)

and 21 December (descending), the earliest flyovers following the earthquake. We generated InSAR interferograms (Figure 2d), consistent to those calculated and provided by other colleagues (methods described in Shea and Barnhart, 2022) (William Barnhart, personal communication), which helped focus our search for surface deformation on 17 December. The images showed the presence of two linear discontinuities in the interferograms, potentially related to ground movement, including an ∼2-km-long ENE-trending lineament about 2.5 km south of the epicenter and east of the Walker River, and an ∼11-km-long NW-trending lineament along the western side of Campbell Valley (Figure 2d).

Surface evidence of ground disturbance was not observed along several walking transects across the ENE-trending InSAR lineament (Figures 2c and 2d), which aligns with the aftershocks and the interpreted buried rupture (Figure 2b). However, a continuous ∼1.5-km-long surface fracture array was identified along the NW-trending InSAR lineament extending between coordinates 39.0905, -118.9866 and 39.1006, -118.9960 (Figure 3). Field photos of the fractures are shown in Figure 4. The geometric pattern is consistent with NNW-striking opening-mode fractures accommodating overall right-lateral displacement across the NW-trending zone. The fracture array trace trends 315° and is characterized by left-stepping en echelon and overlapping extensional-dextral fractures oriented 340° (Figures 4a-4c). Individual fractures range in length from 10 to 20 m and are separated by 1- to 3-m-wide steps. Short subsidiary fractures trending 000°–350° occur within the steps. The fractures diminish in length and opening widths at the ends of the fracture array. Similar surface fracture patterns have been produced in moderate magnitude earthquakes by seismic slip (e.g. 2020 Monte Cristo; Koehler et al., 2021) and triggered creep (e.g. 2004 Parkfield; Rymer et al., 2006). Although the offset across individual fractures was variable and predominantly characterized by ∼1-cm-wide openings, right-lateral displacements of 2–5 cm were observed in several locations (Figure 4a). Similar fractures were not observed along several additional transects to the southeast along the NW-trending lineament revealed by the InSAR. Fractures tapered to undetectable at the NW end of the mapped zone (Figures 2c and 3), so we ended our exploration there, however, we cannot preclude the presence of additional fractures to the NW. As a result, we constrain a minimum length of the surface fracture array of 1.5 km.

Aerial photographs were acquired along the surface fracture array observed in the field (1.205 km^2 coverage) using a DJI Phantom 4 Pro UAS flown with side and forward image overlap of 70% and 80%, respectively. The mission altitude was 50 m above the ground surface, resulting in a spatial resolution of 1.86 cm/pixel with the 20 megapixel camera. Pix4d Structure from Motion software was used to produce a georeferenced digital surface model and an orthophoto mosaic (Figure 4c; Supplemental Section S1).

The orthophoto mosaic (Figure 4c) provides some aerial documentation of the left-stepping and anastomosing pattern of the fractures observed in the field. We found that the individual fractures were generally not observable on the digital surface model (DSM) due to the small size of the extensional opening mode cracks. Fractures extending through clusters of sagebrush were not observable on the DSM and the orthophoto mosaic. In several locations where direct observations were made in the field, fractures could be confidently identified on the orthophoto mosaic (Figure 4c) primarily where the fractures were $\gtrsim$2 cm-wide, which represents the detection limit at this resolution. It is also possible that several rain events that occurred after the earthquake and prior to our aerial survey diminished the sharpness of the fracture margins, further inhibiting their detection on the image.

3.4 Secondary effects of earthquake shaking

We observed bank failures, lateral spread, and liquefaction-related sand blows along the Walker River, as well as isolated mass-wasting features (soil and rock topples and falls, and debris talus cones) along steep bluffs, quarry exposures, and channel margins (Figure 2c). These features are interpreted to be secondary effects of earthquake shaking that occurred coseismically because they buried living vegetation and have sharp geomorphic expression. Numerous boulders and cobbles embedded in a polygonally cracked silt playa surface near the epicenter displayed no evidence of displacement (toppling or flipping over; c.f. Zuckerman et al., 2020), (Figure 2c, 39.1690, -119.0357), suggesting that the vertical ground acceleration was of insufficient amplitude or duration to induce upward acceleration of cobbles.

The displacement of fragile geologic features is sensitive to both the strength and the frequency content of the ground motion (e.g. Purvance et al., 2008), which can limit the toppling efficiency in the near field of a moderate earthquake, where the shaking is concentrated at relatively high frequencies (Trugman et al., 2023). We calculated the median expected PGA and PGV for each of the observation points shown on Figure 2c (Supplemental Section S2) based on the distance to the rupture plane, assuming a near-surface site condition of 560 m/s (site class C, very dense soil / soft rock). For these calculations, we use a logarithmic average of the four "active crustal" ground motion models (Abrahamson et al., 2014; Boore et al., 2014; Campbell and Bozorgnia, 2014; Chiou and Youngs, 2014) used in hazard maps for the western US (see Moschetti et al., 2024, for an overview). In general, the results indicate that the sites closest to the rupture experienced ground motions up to 0.4 g and 23 cm/s.

We observed several examples of fresh block collapse of bluffs and riverbanks above the dense aftershock zone. The largest mass wasting feature observed was an approximately 8 by 16 m topple block that shook off the top of a ∼40-m-high bluff of late Pleistocene lacustrine deposits (Figure 5a). Most of the debris consists of intact soil blocks up to 2 m in diameter and smaller rubble and was deposited on the upper half of the talus slope; however, numerous soil blocks up to 1 m

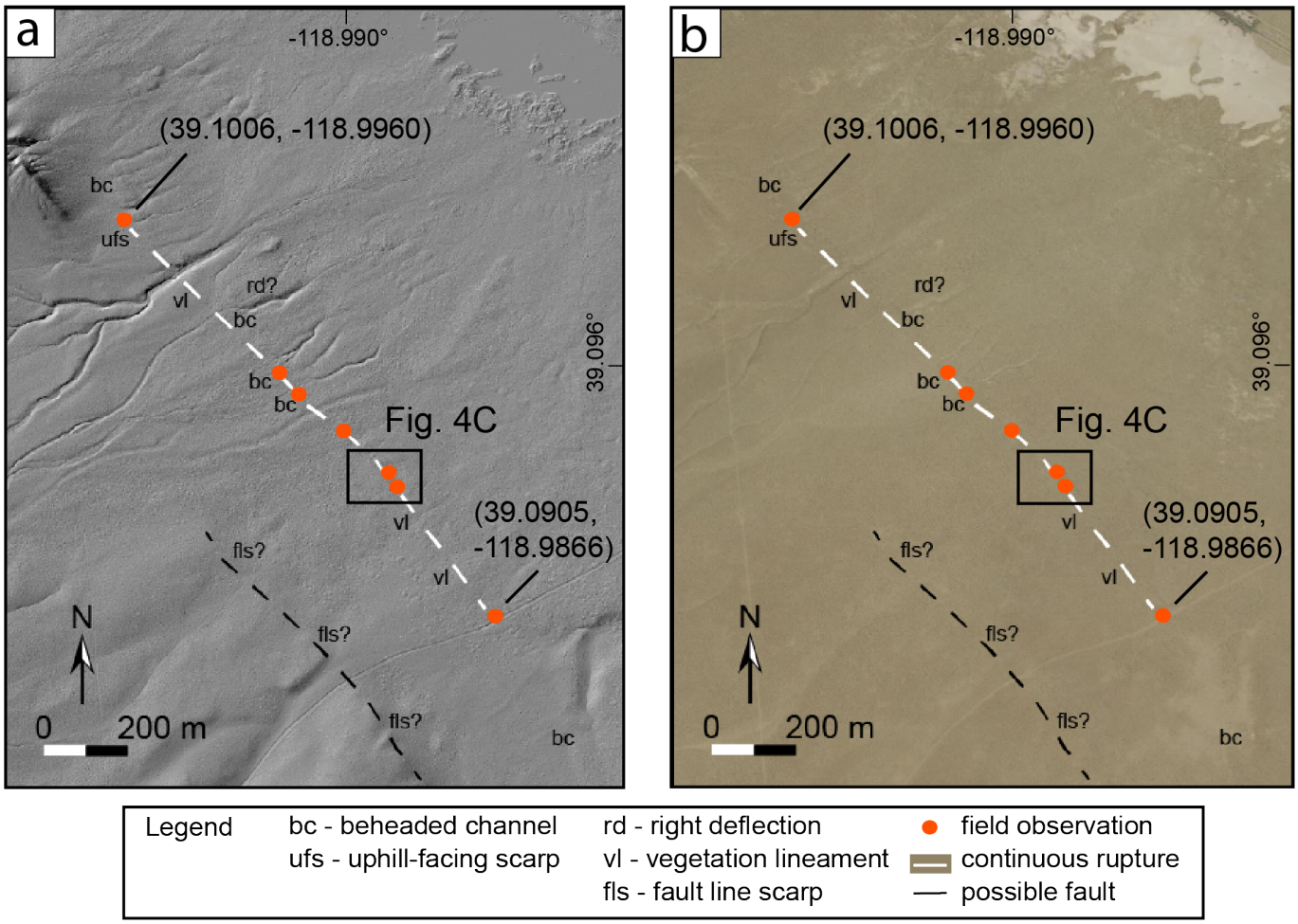

Figure 3 Map of tectonic geomorphic features along the observed surface fracture array including (a) 1-meter bare earth lidar (USGS 3DEP GeoDawn dataset, US Geological Survey, 2023) and (b) aerial imagery (National Agriculture Imagery Program, NAIP, U.S. Department of Agriculture, Farm Services Agency, 2020). Feature abbreviations contained in legend. Red circles are field observation points. White dashed line is generalized trace of surface fracture array that was continuously walked. Black dashed line is possible fault line scarp in bedrock. The aligned features project towards the Wassuk Range fault to the south and a suspected fault observed in a bluff exposure to the north (Figures 2c and 5a). Extent of both panels shown on Figure 2c.

in diameter rolled to the base of the slope burying sage brush and grasses. The largest riverbank failure observed was an approximately 2-m-high by 4-m-long by 0.5-m-wide bank collapse along an outer meander of the Walker River, where the river has cut a Holocene river terrace (Figure 5b). The terrace sediments consisted of weakly consolidated latest Pleistocene lacustrine sediment. The entire height of the bank collapsed, and debris (10s-cm-wide blocks) was deposited at the base of the bank, as well as on frazil ice (collection of loose, randomly oriented ice crystals) anchored along the edge of the river (Figure 5c). Some debris blocks partially broke through the frazil ice, consistent with soft ice conditions at the time of the earthquake (late afternoon), resulting in radiating horizontal ice needles up to 7 cm long forming around the block margins overnight (Figure 5c).

Numerous small earth falls were observed along borrow pit walls in lacustrine sediments and were attributed to earthquake shaking based on burial of accumulated tumbleweeds and living sagebrush (Figure 2c). Indications of where the failures were sourced from the walls was recognized by fresh, loose, and locally damp surfaces as opposed to the 2-mm-thick crust formed by dried rain-washed silt that coats the majority of most exposures of the late Pleistocene lake sediments. These mass failures were typically 0.5–2 m in height, and the debris consisted of intact blocks of weakly coherent sediment up to 30 x 30 cm and rubble piles at the base of steep faces. Small fresh sand and gravel debris fan deposits were also observed along talus slopes in the borrow pits. These fans were sourced from loose latest Pleistocene beach deposits at the top of the exposures and are inferred to have occurred due to shaking because they bury silt-encrusted talus.

Several isolated cobbles on gently-sloping to flat surfaces were moved less than 1 cm from their preserved footprints in weakly indurated soil; however, the majority of rocks (pebbles, cobbles, and boulders) on the surface showed no signs of movement. One boulder approximately 1.2 m x 0.75 m (Figure 5d) in the vicinity of the epicenter toppled out of the stream bank; however, the soil line on its base indicated that it was only embedded ~25 cm into the bank and was thus precarious and particularly susceptible to toppling. All other

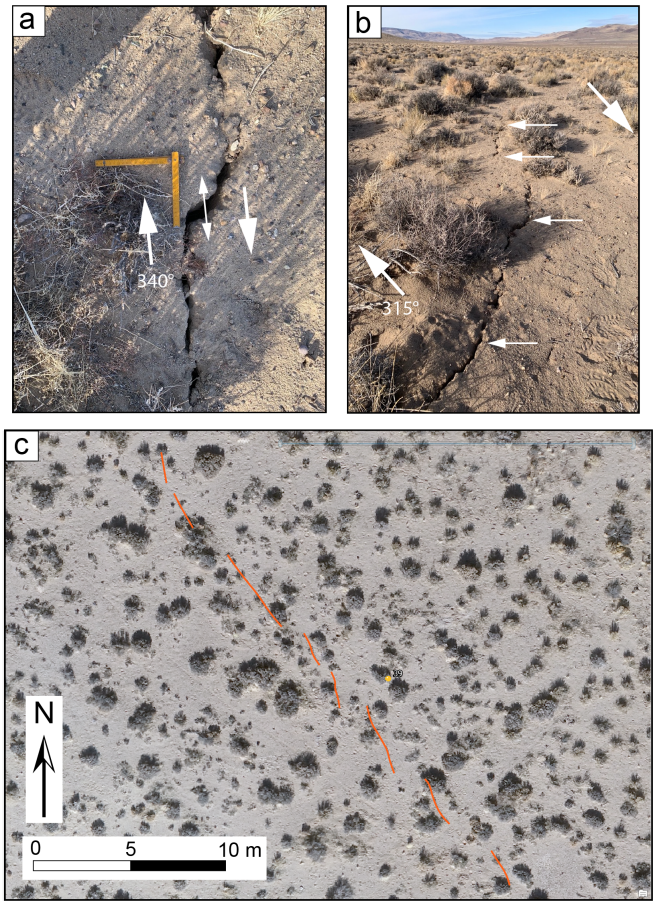

Figure 4 Field photos of surface fractures along the NW-trending InSAR lineament in western Campbell Valley including (a) Right-lateral displacement of about 5 cm along surface fracture striking 340° (39.0940, -118.9892). Folding ruler is 18 cm long. Large arrows and small arrows show right-lateral and extensional opening components, respectively. (b) Left-stepping surface fractures striking 340° (tip of small arrows) within overall 315° striking fracture array (large arrows). View to north (39.0962, -118.9916). Approximate scale of photo in foreground is 2.5 m wide. (c) Orthophoto mosaic generated from the drone survey showing left stepping surface fractures (red lines) (coordinates of yellow circle: 39.0940, -118.9892). See Supplemental Section S1 for full extent of photomosaic.

boulders observed protruding out of the stream bank, as well as on the adjacent Holocene alluvial fan surface observed during our 0.5-km-long walking transect near the epicenter, did not move.

Sand blows and vented sand along opening-mode cracks developed during lateral spreading were observed along the Walker River. Lateral spreading was observed along ~30 m of the riverbank where the bank was about 1–1.5 m above current river level (Figure 6a). The cracks were sub-parallel to the river and manifested as wedge-shaped open cracks 2–6 cm wide and up to 25 cm deep in clean, fine sand, with pure opening mode displacement. Cracks were present but poorly developed in muddy sand and gravels. The longest crack measured was approximately 30 m. Cracks at this site trend 220°. Most cracks are not associated with ejected sand, but some patchy sand deposits were observed within and adjacent to the widest crack (Figure 6a). The ejected sand deposit covered the layer of cottonwood leaves blanketing the ground around the river.

We observed sand blows 35–75 cm long and ~15 cm high at three locations close to the river on cut terraces within 2 m of the river elevation but at varying distances to the active channel (generally within 50 m). The sand deposits are circular to elliptical in map view and overlie the blanket of fallen cottonwood leaves and grasses on the riverbanks (Figure 6b). Some had preserved 3–5 cm deep craters at their apexes. Fine to medium moderately well-sorted sand was the dominant liquefied sediment, but in sand blows found nearer to the epicenter, some 0.5–3 cm angular blocks of indurated laminated mud were entrained in the sand blows. The sand blows were sometimes found in clusters of >10 blows a few meters apart, and also found in curvilinear arrays, ~75 m long and sub-parallel to the river. In this case, their distribution may be controlled by sandy source sediments concentrated in ~1 m-wide scroll bars buried in the floodplain. Given that our reconnaissance surveys were not comprehensive, we infer that sand blows were likely common along other low terraces along the Walker River.

In all three locations where fresh sand blows were observed, we also noted deposits of older sand blows, including several examples where newer sand blows erupted through and on top of old deposits, suggesting reactivation of the same source pathways. The older sand blows were distinguished by weathering, thin mud drapes, thick rain crusts, and sometimes plants growing directly in the craters or through the edges of the deposits. The fresh sand blows overtopped and buried small forbs and grasses, were brighter in color, and had soft loose surfaces with grains easily mobilized by the breeze, without any rain crusts. It is not known whether the older generation of sand blows might have formed during the closest known historical earthquake (Wabuska >M6, 1933; Slemmons et al., 1965), in an earlier event in the immediate vicinity, or a larger, more distal earthquake, but the repetition indicates favorable conditions for liquefaction along the Walker River floodplain.

3.5 Evidence of older faulting

We observed evidence of potential older faulting in the high bluff whose face is approximately perpendicular to the ENE-striking aftershock zone and inferred mainshock rupture plane of the 9 December earthquake, which experienced block collapse due to shaking (Figure 5a). The bluff exposure consists of pluvial Lake Lahontan sediments that are shallowly dipping on the north side of the exposure and sharply juxtaposed against more steeply dipping deposits on the south side (Figure 5a), suggesting the possible presence of a fault at a high angle to the bluff. However, slope debris, including talus as well as landslide debris generated by the earthquake, prevented direct observation of the contact, and its orientation is unknown. The dip discontinuity in the old lake deposits is overlain by a well-developed soil that is not displaced and is buried by

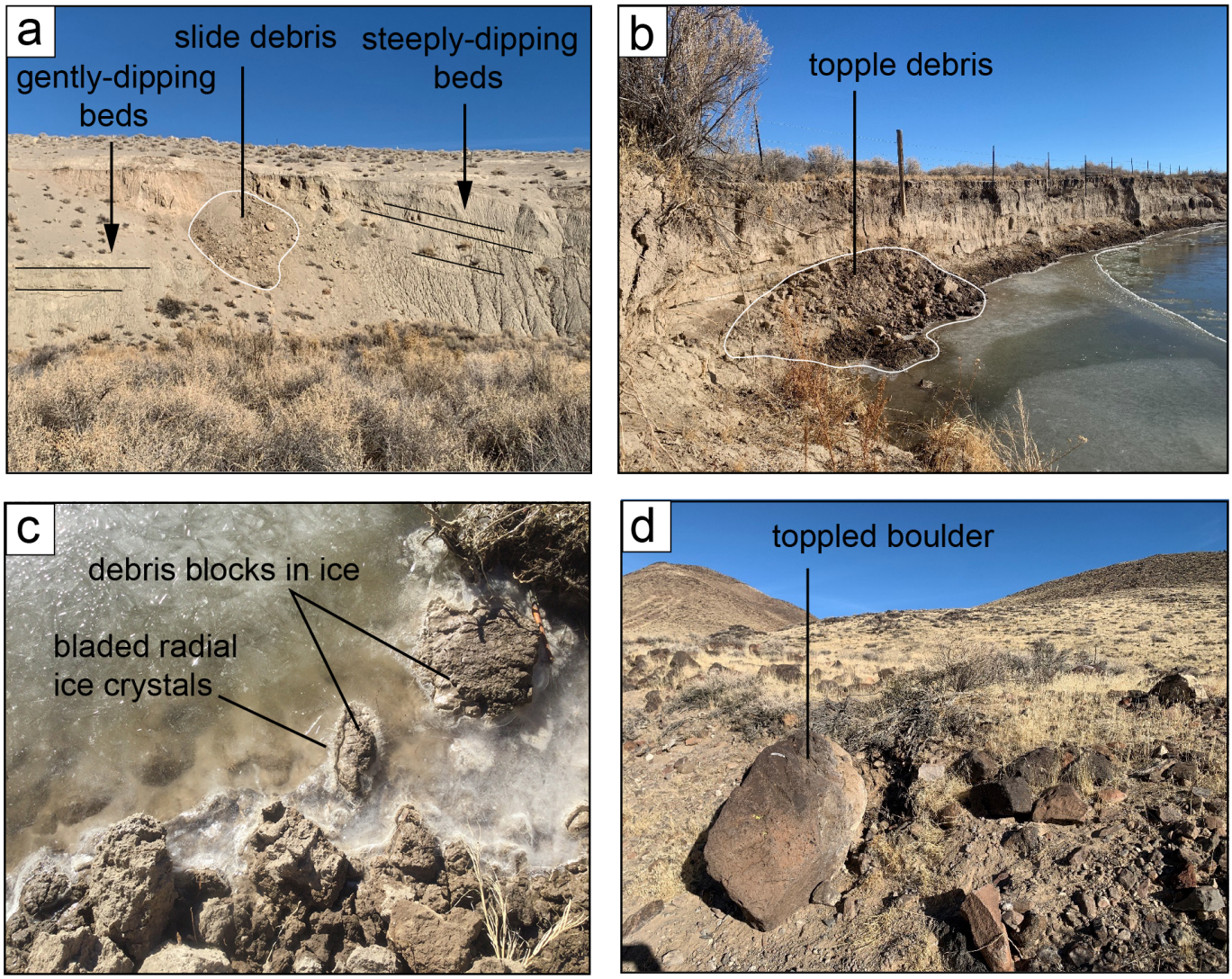

Figure 5 Field photos of secondary shaking effects. (a) West facing bluff within the aftershock zone west of epicenter. Block fall debris mantles the center of the slope (white polygon). Relatively flat-lying lacustrine beds on the left and dipping beds on the right (black lines) suggest a possible fault along strike of the aftershock pattern (39.1576, -119.0422). (b) Bank failure debris along the Walker River (center left, white polygon). Toe of debris broke through ice suggesting that the ice was soft in the late afternoon at the time of the earthquake (39.1598, -119.0778). (c) Close-up view of debris blocks partially embedded in frazil ice along the margin of the river at photo in (b). (d) Toppled basalt boulder shaken out of a wash margin east of the epicenter. Soil line (beige color) along right side of boulder indicates shallow burial depth (39.1832, -119.0170).

un-faulted, latest Pleistocene lacustrine deposits. If the interpretation of the discontinuity as a fault is correct (and not a channel fill in the lake deposits), the observations are consistent with the lack of surficial geomorphologic indicators of faulting (i.e., the most recent surface displacement on this fault pre-dates the un-faulted latest Pleistocene deposits). The relations may represent Pleistocene surface displacement on the same or similar fault that ruptured only at depth on 9 December. Another possibility is that this could be a NW-striking fault coincident with the InSAR discontinuity (Figure 2d). In either case, the relations suggest a period of quiescence on the order of ~10s ka or longer. Observations in the bluff exposure of older convolute bedding and slump folds in lake beds buried by conformable lake strata also indicate that significant local seismic shaking occurred during Lake Lahontan time (>15.5 cal. YBP).

3.6 Geotechnical and infrastructure observations

A bridge across the Walker River along a power line maintenance road with concrete abutments buried in fill was observed to have minor settlement and cracking along the abutment/fill interface, but no cracking was observed in the concrete (Figure 6c). The alignment of power line transmission towers extending north and south of the bridge did not appear to be affected. The cracks align along the boundary between the concrete abutments and the fill, which consists of poorly consolidated sedimentary material locally sourced from the river terraces. Separations are only opening mode and 0.5–3 cm wide along the edges of the sediment where it contacts the abutments. The cracks terminate less than a meter away from the abutment corners. The cracks were fresh when observed on 10 December as indicated by dangling thin living roots of grasses, sharp

corners with 1–3 mm-thick dry soil crust on the top of the soil dangling over the open cracks. To the south of the bridge, an open crack up to 2 cm wide runs down the center of the road from the end of the abutment for approximately 40 m. We noted no indication of damage or instability to the bridge abutments themselves, with the cracking confined to the unconsolidated fill along the abutment interface. The cracks are inferred to be related to cyclic lateral movements of the abutments and/or consolidation settlement of the fill material.

Beneath the bridge on the south side, we observed slumping of the riverbank within the fill prism against the abutment, extending ∼5 m to the west within river terrace deposits (Figure 6d). The slumping was associated with bank-parallel opening mode cracks up to 15 cm wide cutting dry sediment, frozen sediment, and floating river ice. Water froze into the cracks with long, crack-spanning bladed crystals, suggesting rapid freezing overnight following the late afternoon failure. The slumping may have also contributed towards the cracking at the abutment fill interface upslope by reducing basal support of the fill prism.

The Wabuska geothermal system resides in a structurally complex displacement transfer zone (Faulds et al., 2021) within the epicentral region of the Parker Butte earthquake. The Wabuska Geothermal Power Plant (see Figure 1 for location), currently operated by Open Mountain Energy, is a binary facility with a nameplate capacity of 6.4 MWe (Jowitt et al., 2024) located about 13 km due west of the epicenter. No significant impacts were observed to the geothermal resource and peak ground accelerations were low (∼0.1 g) (Julian Lane site, Supplementary Section S2, Table S2-1). The plant had been offline for brief periods before and following the earthquake, so some well data collection was disrupted, making it challenging to identify any potential subtle changes in pressure, temperature, or fluid flow that may have occurred in response to the earthquake. The plant experienced negligible impacts to surface equipment, and operations at the plant have continued as they were prior to the earthquake (Casteel, J. personal communication, December 12, 2024).

3.7 Temperature and ice observations

In early December, the Mason Valley was dry, sunny and cold during the days, with temperatures dropping below freezing overnight. These weather conditions resulted in the potential for delicate deformation features caused by seismic shaking to be temporarily preserved in ice, which were observed during field reconnaissance on the morning after the earthquake. On the day of the mainshock, the high temperature was 8°C about an hour before the mainshock at 15:08, and the temperature fell to the overnight low of -8°C at 07:00 on 10 December, while the Walker River discharge reduced slightly overnight (from 58 to 47 cfs).

Cracked and disturbed ice was observed in several agricultural ditches (Figure 6e) and the Walker River (Figures 5b and 5c). Crack patterns and surficial ice characteristics suggest partial melting and refreezing of the ice after the earthquake. An irrigation channel oriented subparallel to the mainshock plane (trend ∼260°) contained bank-parallel longitudinal cracks, healed with ridges of frozen frazil slush (slush made from angular millimetric to centimetric shards of ice formed in fast moving water), which could have been formed by surface waves disturbing the floating ice sheet or by cracking of the frozen surface in response to lowering of the river level downstream during the night. A branch channel oriented at about 45° to the mainshock plane contained cracks trending ∼260° as well as bank-parallel cracks trending toward 315°. These cracks were healed with long (5–15 cm) bladed ice crystals rather than frazil slush, consistent with still water underneath the frozen surface in the tributary channel. The two orientations may differentiate the mechanism of cracking: the channel-parallel set (315°) due to water level changes and the rupture-parallel set (260°) caused by surface waves from the earthquake. A similar suggestion of cracking reflecting seismic wave propagation fields arose from observations of coseismic cracking and subsequent healing of lake ice in two M∼6 2002 earthquakes in Türkiye (Yürür et al., 2003).

4 Discussion and Conclusions

The Parker Butte earthquake occurred along a previously unmapped ENE-trending fault in the central Walker Lane and was not observed to be associated with surface rupture. However, a NW-trending lineament south of the mainshock was identified in InSAR interferograms 8 days after the mainshock and was confirmed by field observation to be associated with surface displacement. The presence of this surface displacement is unexpected given the distributed, low-density aftershock pattern along the lineament and lack of surface rupture associated with the mainshock. These features indicate shallow slip along a fault orthogonal to the main rupture, either co-seismically, or during post-seismic slip/creep.

Although the mechanism responsible for the left-stepping en echelon fractures observed along the NW-trending InSAR lineament was not evident during the post-event field surveys, subsequent fault modeling of the event based on geodetic inversions and Coulomb stress changes indicates that slip on the NE-SW-striking main fault promoted failure at depth and aseismic slip (or afterslip) on the NW-SE-striking plane (Bogolub et al., 2025). The geometric pattern and cm-scale openings of the fractures observed on the surface are consistent with right-lateral slip and similar to fractures generated in other moderate magnitude strike-slip earthquakes. Although this type of deformation has been associated with coseismic surface fault rupture (e.g. 2020 Monte Cristo, Koehler et al., 2021), a variety of other mechanisms including afterslip and creep can generate similar features. Creep meter array analyses of the 2004 Parkfield (M6.0) earthquake along the San Andreas fault indicated that coseismic slip was <0.2 cm with 3-6 cm of afterslip occuring in the first 24 hours (Lienkaemper et al., 2006). This slip was expressed as left-stepping en echelon fractures as observed in field surveys (Rymer et al., 2006). Based on orthophoto mosaics and 3-D to-

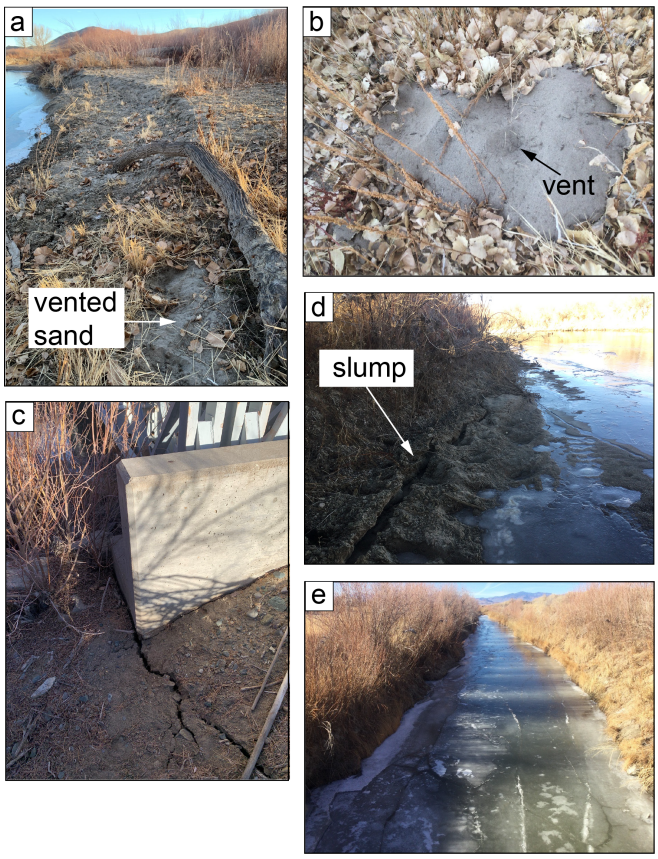

Figure 6 Field photos of secondary shaking effects. (a) Zone of lateral spreading along the bank of the Walker River. Pockets of sand ejecta (bottom right) bury leaf litter (39.1560, -119.0863). (b) Liquefaction-related sand boil along bank of Walker River. Collapsed vent is in the center of the deposit. Sand cleared away on left to demonstrate leaf litter buried by the sand (39.1571, -119.0864). (c) Power line road bridge over the Walker River. Cracking and separation (up to 3 cm) of fill from south concrete abutment. (39.1587, -119.0515). (d) Riverbank slump in terrace deposits below south abutment of power line road bridge (39.1585, -119.0517). (e) Cracked and healed ice in frozen drainage ditch (39.1514, -119.1042).

pographic differencing, Scott et al. (2020) mapped left-stepping en echelon fractures along the Parkfield section of the San Andreas fault at Dry Lake Valley. Scott et al. (2020) estimated that the fractures accommodated ~2.2 cm/yr of right slip and attributed their formation and preservation to creep during dry conditions (drought between 2012 and 2014). Creep is further substantiated in this area by upward splaying clay shear bands that extend to the surface and cm-scale filled fissures exposed in paleoseismic trenches (Toké et al., 2006; Toké and Arrowsmith, 2015).

Neither the mainshock (ENE-trending vertical fault) nor the NW-trending surface fracture trace are well-aligned with any previously mapped faults, although similarly oriented active faults are known from the adjacent range fronts (Figure 1). Inspection of lidar hillshades and satellite imagery show subtle geomorphic features indicative of fault offset along the trace of the NW-trending lineament including uphill facing scarps, beheaded channels, fault line scarps in bedrock, vegetation lineaments, and possible stream deflections (Figure 3). Additionally, the lineament projects to the suspected fault observed in the bluff exposure to the north (Figures 2c and 5a). The observed surface fracture array is entirely below the elevation of the highstand of pluvial Lake Lahontan, which may have buried or eroded evidence of prior surface displacements. Although this fault has not been recognized in previous mapping efforts, it is subparallel to several faults mapped in the valley and along strike with the northern continuation of the Wassuk Range fault (Figure 1). Whether the slip which caused the surface fractures occurred on the buried continuation of the Wassuk Range fault, and whether it can independently rupture in earthquakes, are unresolved questions.

The Parker Butte earthquake and its aftershock pattern, as well as the high-angle orientation of the surface fracture trace to the mainshock fault plane, are similar to other previous earthquake pairs in the region and may represent a significant mechanism of strain release in the central Walker Lane. Co-seismic rupture along faults that intersect at high angles (~80-90°) has been observed in nearly every moderate to strong earthquake sequence in the Walker Lane over the last 45 years. These include the 1980 Long Valley, 1984 M5.9 Round Valley, 1986 M6.3 Chalfant, 1994 Mw5.8 Double Spring Flat, 2016 Mw5.4-5.6 Nine Mile Ranch, 2019 Mw7.1 and Mw6.4 Ridgecrest, and 2020 Mw6.5 Monte Cristo Range earthquake sequences (Hill, 2006; Smith and Priestly, 1993, 2000; Ichinose et al., 1998; Ponti et al., 2020; Koehler et al., 2021; Hatch-Ibarra et al., 2022). These earthquakes all involved rupture on intersecting left- and right-lateral strike-slip faults and have typically been referred to as conjugate ruptures, cross-fault ruptures, and/or orthogonal ruptures in the literature. Additionally, possible orthogonal faulting has been inferred from paleoseismic records from the Dog Valley and Polaris faults north of Lake Tahoe (Pierce and Koehler, 2023). The relatively common occurrence of orthogonal ruptures in the Walker Lane has raised awareness of the potential for static stress changes that could result in triggering larger earthquakes. This process is analogous to the 2019 Ridgecrest, California earthquakes where the July 4th Mw6.4 northeast-striking left-lateral rupture (foreshock) occurred ~34 hours prior to the July 5th Mw7.1 northwest-striking right-lateral rupture (Ponti et al., 2020; DuRoss et al., 2020). Static stress change analysis of these events showed that the foreshock sequence systematically promoted slip at the Mw7.1 hypocenter suggesting that static stress changes play an important role in the genesis of cross-fault ruptures (Barnhart et al., 2019).

Post-event field reconnaissance provides essential on-the-ground observations of surface displacement and secondary effects that serve to validate and complement geodetic remote sensing and seismological observations. Remote observation techniques such as post-event lidar, InSAR, and pixel correlation on satellite imagery, as well as a better understanding of the field evidence of surface rupture in moderate earthquakes and creep events, have enhanced the ability to locate and measure small (cm-scale) surface defor-

mation. As these technologies have evolved, observations of surface rupture and/or fracturing in moderate magnitude earthquakes (< M6) have become increasingly recognized. For example, the 2020 Mw5.1 Sparta earthquake in North Carolina generated a 2-km-long zone of traceable reverse displacements averaging 8-10-cm-high that were first recognized in the field and subsequently mapped in detail using post-event lidar (Figueiredo et al., 2022). InSAR interferograms were instrumental in locating 5-20 cm lateral displacements up to 10 km west of the epicenter in the 2020 Mw 6.5 Monte Cristo Range, Nevada earthquake (Koehler et al., 2021); however, many InSAR discontinuities interpreted in the office as possible ruptures showed no signs of deformation in the field (some possibly related to sloughing of terrace riser escarpments, and other processes). Furthermore, the detailed field mapping of the Monte Cristo ruptures proved more effective than the InSAR at recognizing wide zones (up to 800-m-wide) comprised of hundreds of centimeter scale extensional fractures (Koehler et al., 2021; Dee et al., 2021). In the case of the Parker Butte earthquake, the recognition of surface fracturing was entirely attributable to the InSAR observations, which motivated expanding the area of field reconnaissance outside the zone of concentrated aftershocks. Notably, and similar to the Monte Cristo example, we only observed surface deformation on one of the two InSAR discontinuities. Additionally, we were able to measure the scale of the displacements in the field at a level of detail that the InSAR could not. Thus, in both the Monte Cristo and Parker Butte earthquake surveys, the combination of rapid field deployment and quick availability of the InSAR scenes led to comprehensive documentation of perishable displacement features, reinforcing the need for multidisciplinary responses in future earthquakes. This also holds true for large magnitude events such as the 2023 Kahramanmaras, Türkiye earthquakes where carefully planned field reconnaissance was able to resolve surface displacements and rupture geometry complexities in areas with obscured and/or low resolution remote data (DuRoss et al., 2025).

The minor fracturing documented in the Parker Butte earthquake contributes to global surface rupture datasets that are the basis for scaling relationships of displacement vs. magnitude used in seismic hazards assessments, which like our work has benefited from joint analysis of field and satellite radar observations (Brengman et al., 2019). Of the 421 events (strike slip, normal, and reverse) used by Wells and Coppersmith (1994), only 70 events were of a magnitude M<6 and the majority of these events were not associated with measurements of surface displacement. In more recent evaluations of scaling relationships, Anderson et al. (2021) considered 55 strike-slip earthquakes, with only two of which being of magnitude M<6, and Stirling et al. (2024) restricted their database to earthquakes M>7. Thus, documenting surface rupture in moderate earthquakes contributes to global datasets and is important for future refinements of scaling relationships. However, the scaling relationship may break down at lower magnitudes where the surface displacement will be more sensitive to the depth of maximum slip.

Our efforts also highlight the importance of multidisciplinary responses to earthquakes, including geology, seismology, remote sensing, and public awareness. The secondary shaking effects documented in our reconnaissance surveys are typical features expected for an earthquake of this size. Although the effects were relatively minor in size and distribution, the perishable nature of these features makes rapid documentation imperative. The knowledge gained from documenting the earthquake effects contributes to a better understanding of potential effects related to future moderate earthquakes and has implications for engineering geologic practice and public safety. The documentation of transient shaking damage features in river ice is, as far as we know, novel and dependent on specific weather conditions, but with better understanding, this may represent a new line of potential evidence for revealing shaking effects from earthquakes.

Acknowledgements

Rapid deployment of seismic stations by the Nevada Seismological Laboratory field staff enabled better resolution of mainshock and aftershock locations for this summary and future studies – we thank Will Honjas, Andrew Rosenberg-Main, Ryan Brandani, Jackson Mendelsohn, Brandon Bell, Matt Barnard, Bill Savran, Ian Scoggin, Austin Armstrong, Quinn O'Neil, and Hannah Martin for the accelerated effort. Our field reconnaissance of the epicentral area was supported by operational funds provided by the Nevada Bureau of Mines and Geology and the Nevada Seismological Laboratory. Daniel Trugman and Yu Jiang gratefully acknowledge support for this study from National Aeronautics and Space Administration (NASA) Earth Surface and Interiors Award 80NSSC24K0736 and Nevada Division of Emergency Management Award HMGP DR-4523-08-08P. Hammond was supported for collection of data in the MAGNET GPS network by the USGS Geodetic Networks Program cooperative agreement G24AC00183. Processing of GPS data was supported by NASA project 80NSSC25K7895. Support for the collection and analysis of seismic data from the Nevada Seismological Laboratory's seismic network including the temporary network of aftershock kits was provided by the USGS ANSS cooperative agreement G25AC00163. We would also like to thank the USGS for providing the rapid deployment kits to study the aftershock sequences. We thank G. Castle, and C. Beadell of the Center for Transformative Environmental Sensing Programs at UNR for assistance in acquiring the drone data. We thank S. Wesnousky (NSL) for helpful comments and J. Casteel at the Wabuska Geothermal Power Plant for discussing the shaking effects. We also thank Nathan Toke, an anonymous reviewer, and Seismica editor Alexandra Hatem for insightful comments that improved the content. Additionally, we thank R. Briggs and W. Barnhart of the U.S. Geological Survey for providing timely InSAR interferograms and interpretations which helped focus our reconnaissance efforts.

Data and code availability

All data used in this study are publicly available including (1) seismicity and InSAR data from the Nevada Seismological Laboratory, (2) geodetic data from the Nevada Geodetic Laboratory, and (3) field observations and photographs from the Nevada Bureau of Mines and Geology. Shapefiles for digital surface model (DSM) and orthophoto mosaic, as well as KMZ files indicating field observations are downloadable on the Nevada Bureau of Mines and Geology Earthquake Clearinghouse webpage at https://nevada-earthquake-clearinghouse-nbmg.hub.arcgis.com/pages/parker-butte-earthquake with additional galleries of field photos.

Competing interests

The authors have no competing interests.

References

Abrahamson, N. A., Silva, W. J., and Kamai, R. Summary of the ASK14 ground motion relation for active crustal regions. *Earthquake Spectra*, 30(3):1025–1055, 2014. doi: 10.1193/070913EQS198M.

Anderson, J., Biasi, G., Agster, S., and Wesnousky, S. Improved scaling relationships for seismic moment and average slip of strike-slip earthquakes incorporating fault-slip rate, fault width, and stress drop. *Bulletin of the Seismological Society of America*, 111 (5):2379–2392, 2021. doi: 10.1785/0120210113.

Angster, S., Wesnousky, S., Figueredo, P., Owen, L., and Hammer, S. Late Quaternary slip rates for faults of the central Walker Lane: Spatiotemporal strain release in a strike-slip fault system. *Geosphere*, 15(5):1460–1478, 2019. doi: 10.1130/GES02088.1.

Barnhart, W. D., Hayes, G. P., and Gold, R. D. The July 2019 Ridgecrest, California, earthquake sequence: Kinematics of slip and stressing in cross-fault ruptures. *Geophysical Research Letters*, 46(21):11859–11867, 2019. doi: 10.1029/2019GL084741.

Bogolub, K. R., Trugman, D. T., Jiang, Y., Hammond, W. C., Smith, K. D., Koehler, R. D., and Rowe, C. D. The M 5.7 Parker Butte Earthquake near Yerington, Nevada: Anatomy of a Dual-Plane Rupture in the Walker Lane from high-precision relocated earthquakes, InSAR, GPS and Strong Motion Data. *Seismological Research Letters*, 2025. doi: 10.1785/0220250203.

Boore, D. M., Stewart, J. P., Seyhan, E., and Atkinson, G. M. NGA-West2 equations for predicting PGA, PGV, and 5% damped PSA for shallow crustal earthquakes. *Earthquake Spectra*, 30(3): 1057–1085, 2014. doi: 10.1193/070113EQS184M.

Bormann, J., Hammond, W., Kreemer, C., and Blewitt, G. Accommodation of missing shear strain in the Central Walker Lane, western North America: Constraints from dense GPS measurements. *Earth and Planetary Science Letters*, 440:169–177, 2016. doi: 10.1016/j.epsl.2016.01.015.

Bormann, J. M., Surpless, B. E., Caffee, M. W., and Wesnousky, S. G. Holocene earthquakes and late Pleistocene slip-rate estimates on the Wassuk Range fault zone, Nevada. *Bulletin of the Seismological Society of America*, 102(4):1884–1891, 2012. doi: 10.1785/0120110287.

Brengman, C. M., Barnhart, W. D., Mankin, E. H., and Miller, C. N. Earthquake-scaling relationships from geodetically derived slip distributions. *Bulletin of the Seismological Society of America*, 109(5):1701–1715, 2019. doi: 10.1785/0120190048.

Callaghan, E. and Gianella, V. The earthquake of January 30, 1934, at Excelsior Mountains, Nevada. *Bulletin of the Seismological Society of America*, 25:161–168, 1935. doi: 10.1785/BSSA0250020161.

Campbell, K. W. and Bozorgnia, Y. NGA-West2 ground motion model for the average horizontal components of PGA, PGV, and 5% damped linear acceleration response spectra. *Earthquake Spectra*, 30(3):1087–1115, 2014. doi: 10.1193/062913EQS175M.

Cashman, P. and Fontaine, S. Strain partitioning in the northern Walker Lane, western Nevada and northeastern California. *Tectonophysics*, 326:111–130, 2000. doi: 10.1016/S0040-1951(00)00149-9.

Chiou, B. S.-J. and Youngs, R. R. Update of the Chiou and Youngs NGA model for the average horizontal component of peak ground motion and response spectra. *Earthquake Spectra*, 30(3):1117–1153, 2014. doi: 10.1193/072813EQS21.

Dee, S., Koehler, R., Elliott, A., Hatem, A., Pickering, A., Pierce, I., Seitz, G., Collett, C., Dawson, T., De Masi, C., dePolo, C., Hartshorn, E., Madugo, C., Trexler, C., Verdugo, D., Wesnousky, S., and Zachariasen, J. Surface rupture map of the 2020 M6.5 Monte Cristo Range earthquake, Esmeralda and Mineral counties, Nevada. Technical report, Nevada Bureau of Mines and Geology Map 190: 2 sheets, scale 1:14,000, 2021.

dePolo, D. and dePolo, C. Earthquakes in Nevada: 1840's to 2010. Technical report, Nevada Bureau of Mines and Geology, Map 179, scale 1:1,000,000, 2012.

Dong, S., Ucarkus, G., Wesnousky, S., Maloney, J., Kent, G., Driscoll, N., and Baskin, R. Strike-slip faulting along the Wassuk Range of the northern Walker Lane, Nevada. *Geosphere*, 10(1):9, 2014. doi: 10.1130/GES00912.1.

DuRoss, C. B., Gold, R. D., Dawson, T. E., Scharer, K. M., Kendrick, K. J., Akciz, S. O., Angster, S. J., Bachhuber, J., Bacon, S., Bennett, S. E., et al. Surface displacement distributions for the July 2019 Ridgecrest, California, earthquake ruptures. *Bulletin of the Seismological Society of America*, 110(4):1400–1418, 2020. doi: 10.1785/0120200058.

DuRoss, C. B., Reitman, N. G., Hatem, A. E., Mason, H. B., Lavrentiadis, G., Asimaki, D., Milliner, C., Karakaş, M., and Seçen, B. Are Field Observations of Surface Rupture Useful? An Example from the 2023 M w 7.8 Pazarcık, Turkey (Türkiye), Earthquake. *Seismological Research Letters*, 96(2A):848–867, 2025. doi: 10.1785/0220240280.

Faulds, J., Coolbaugh, M., and Hinz, N. Inventory of structural settings for active geothermal systems and late Miocene (∼8 Ma) to Quaternary epithermal mineral deposits in the Basin and Range province of Nevada. Technical Report Report 58, Nevada Bureau of Mines and Geology, 2021. 3 plates, scale 1:2,500,000.

Figueiredo, P., Hill, J., Merschat, A., Scheip, C., Stewart, K., Owen, L., Wooten, R., Carter, M., Szymanski, E., Horton, S., Wegmann, K., Bohnenstiehl, D., Thompson, G., Witt, A., Cattanach, B., and Douglas, T. The Mw5.1, 9 August 2020, Sparta earthquake, North Carolina: The first documented seismic surface rupture in the eastern United States. *GSA Today*, 32:4–11, 2022. doi: 10.1130/GSATG517A.1.

Hammond, W. and Thatcher, W. Crustal deformation across the Sierra Nevada, northern Walker Lane, Basin and Range transition, western United States measured with GPS, 2000–2004. *Journal of Geophysical Research*, 112, 2007. doi: 10.1029/2006JB004625.

Hammond, W. C., Kreemer, C., and Blewitt, G. Robust imaging of fault slip rates in the Walker Lane and western Great Basin from GPS data using a multi-block model approach. *Journal of Geophysical Research: Solid Earth*, 129(3):e2023JB028044, 2024. doi: 10.1029/2023JB028044.

Hatch-Ibarra, R., Abercrombie, R., Ruhl, C., Smith, I., Hammond, W., and Pierce, I. The 2016 Nine Mile Ranch earthquakes: Hazard and tectonic implications of orthogonal conjugate faulting in the Walker Lane. *Bulletin of the Seismological Society of America*, 112:1727–1741, 2022. doi: 10.1785/0120210149.

Hill, D. Unrest in Long Valley Caldera, California, 1978-2004. In Troise, C., De Natale, G., and Kilburn, C. R. J., editors, *Mechanisms of activity and unrest at large calderas*, volume 269, pages 1–24. Geological Society, London, 2006. doi: 10.1144/GSL.SP.2006.269.01.02.

Ichinose, G., Smith, K., and Anderson, J. Moment tensor solutions of the 1994 to 1996 Double Spring Flat, Nevada, earthquake sequence and implications for local tectonic models. *Bulletin of the Seismological Society of America*, 88(6):1363–1378, 1998. doi: 10.1785/BSSA0880061363.

Jowitt, S., Micander, R., Richards, M., Fisher, T., Reynolds, D., and Lu, C. *The Nevada Mineral Industry 2023*. Open-File Report. Nevada Bureau of Mines and Geology, 2024.

Koehler, R., Dee, S., Elliott, A., Hatem, A., Pickering, A., Pierce, I., and Seitz, G. Field response and surface rupture characteristics of the 2020 M6.5 Monte Cristo Mountains earthquake, central Walker Lane, Nevada. *Seismological Research Letters*, 92(2A): 823–839, 2021. doi: 10.1785/0220200371.

Li, X., Huang, W., Pierce, I., Angster, S., and Wesnousky, S. Characterizing the Quaternary expression of active faulting along the Olinghouse, Carson, and Wabuska lineament of the Walker Lane. *Geosphere*, 13(6), 2017. doi: 10.1130/GES01483.1.

Lienkaemper, J. J., Baker, B., and McFarland, F. S. Surface slip associated with the 2004 Parkfield, California, earthquake measured on alinement arrays. *Bulletin of the Seismological Society of America*, 96(4B):S239–S249, 2006. doi: 10.1785/0120050806.

Moschetti, M. P., Aagaard, B. T., Ahdi, S. K., Altekruse, J., Boyd, O. S., Frankel, A. D., Herrick, J., Petersen, M. D., Powers, P. M., Rezaeian, S., et al. The 2023 US National Seismic Hazard Model: Ground-motion characterization for the conterminous United States. *Earthquake Spectra*, 40(2):1158–1190, 2024. doi: 10.1177/87552930231223995.

Pierce, I. and Koehler, R. 3D paleoseismology from iOS lidar and Structure from Motion photogrammetry: A case study on the Dog Valley fault, California. *Seismica*, 2(1), 2023. doi: 10.26443/seismica.v2i1.208.

Pierce, I., Wesnousky, S., Owen, L., Bormann, J., Li, X., and Caffee, M. Accommodation of plate motion in an incipient strike-slip system: The central Walker Lane. *Tectonics*, 40:e2019TC005612, 2021. doi: 10.1029/2019TC005612.

Ponti, D. J., Blairm, J. L., Rosa, C. M., Thomas, K., Pickering, A. J., Akciz, S., Angster, S., Avouac, J., Bachhuber, J., Bacon, S., Barth, N., Bennett, S., Blake, K., Bork, S., Brooks, B., Bullard, T., Burgess, P., Chupik, C., Dawson, T., DeFrisco, M., Delano, J., DeLong, S., Dolan, J., Donnellan, A., DuRoss, C., Ericksen, T., Frost, E., Funning, G., Gold, R., Graehl, N., Gutierrez, C., Haddon, E., Hatem, A., Helms, J., Hernandez, J., Hitchcock, C., Holland, P., Hudnut, K., Kendrick, K., Koehler, R., Kozaci, O., Ladinsky, T., Leeper, R., Madugo, C., Mareschal, M., McDonald, J., McPhillips, D., Milliner, C., Mongovin, D., Morelan, A., Nale, S., Nevitt, J., O'Neal, M., Olson, B., Oskin, M., Padilla, S., Patton, J., Philibosian, B., Pierce, I., Pridmore, C., Roth, N., Sandwell, D., Scharer, K., Seitz, G., Singleton, D., Smith-Konter, B., Spangler, E., Swanson, B., Jobe, J. T., Treiman, J., Valencia, F., Vanderwal, J., Williams, A., Xu, X., Zachariasen, J., Zimmerman, J., and Zinke, R. Documentation of surface fault rupture and ground deformation features produced by the Ridgecrest M6.4 and M7.1 earthquake sequence of July 4 and 5, 2019. *Seismological Research Letters*, 91(5):2942–2959, 2020. doi: 10.1785/0220190322.

Purvance, M. D., Anooshehpoor, A., and Brune, J. N. Freestanding block overturning fragilities: Numerical simulation and experimental validation. *Earthquake Engineering & Structural Dynamics*, 37(5):791–808, 2008.

Rymer, M. J., Tinsley III, J. C., Treiman, J. A., Arrowsmith, J. R., Clahan, K. B., Rosinski, A. M., Bryant, W. A., Snyder, H. A., Fuis, G. S., Toké, N. A., et al. Surface fault slip associated with the 2004 Parkfield, California, earthquake. *Bulletin of the Seismological Society of America*, 96(4B):S11–S27, 2006. doi: 10.1785/0120050830.

Say, M. and Zuza, A. Heterogenous late Miocene extension in the northern Walker Lane (California-Nevada, USA) demonstrates vertically decoupled crustal extension. *Geosphere*, 17(6): 1762–1785, 2021. doi: 10.1130/GES02409.1.

Scott, C., Bunds, M., Shirzaei, M., and Toké, N. Creep along the Central San Andreas Fault from surface fractures, topographic differencing, and InSAR. *Journal of Geophysical Research: Solid Earth*, 125(10):e2020JB019762, 2020. doi: 10.1029/2020JB019762.

Shea, H. N. and Barnhart, W. D. The Geodetic Centroid (gCent) Catalog: Global earthquake monitoring with satellite imaging geodesy. *Bulletin of the Seismological Society of America*, 112 (6):2946–2957, 2022. doi: 10.1785/0120220072.

Slemmons, D., Jones, A., and Gimlett, J. Catalog of Nevada earthquakes. *Bulletin of the Seismological Society of America*, 55(2): 537–583, 1965. doi: 10.1785/BSSA0550020519.

Smith, K. and Priestly, K. Aftershock stress release along active fault planes of the 1984 Round Valley, California earthquake sequence applying a time-domain stress drop method. *Bulletin of the Seismological Society of America*, 83(1):144–159, 1993. doi: 10.1785/BSSA0830010144.

Smith, K. and Priestly, K. Faulting in the 1986 Chalfant, California, sequence: Local tectonics and earthquake source parameters. *Bulletin of the Seismological Society of America*, 90(4):813–831, 2000. doi: 10.1785/0119990129.

Stewart, J. and Ernst, W. Tectonics of the Walker Lane belt, western Great Basin: Mesozoic and Cenozoic deformation in a zone of shear. In Ernst, W. G., editor, *Metamorphism and crustal evolution of the western United States*, volume 7, pages 683–713. Prentice Hall Englewood Cliffs, New Jersey, 1988.

Stirling, M., Fitzgerald, M., Shaw, B., and Ross, C. New magnitude–Area scaling relations for the New Zealand national seismic hazard model 2022. *Bulletin of the Seismological Society of America*, 114(1):137–149, 2024. doi: 10.1785/0120230114.

Toké, N. A., Arrowsmith, J. R., Young, J. J., and Crosby, C. J. Paleoseismic and postseismic observations of surface slip along the Parkfield segment of the San Andreas fault. *Bulletin of the Seismological Society of America*, 96(4B):S221–S238, 2006. doi: 10.1785/0120050809.

Toké, N. A. and Arrowsmith, J. R. Examining the cause of prehistoric ground deformation at the Dry Lake Valley Site along the creeping section of the San Andreas Fault, San Benito, California. Technical report, Southern California Earthquake Center Annual Report #13147, 2015.

Trugman, D., Brune, J., Smith, K., Louie, J., and Kent, G. The rocks that did not fall: A multidisciplinary analysis of near-source ground motions from an active normal fault. *AGU Advances*, 4 (2):e2023AV000885, 2023. doi: 10.1029/2023AV000885.

U.S. Department of Agriculture, Farm Services Agency. National Agriculture Imagery Program (NAIP), 2020. Accessed March 2, 2025, Esri ArcGIS Online.

US Geological Survey. Geoscience Data Acquisition for Western Nevada (GeoDAWN) project, 3D Elevation Program (3DEP), DOE Geothermal Technologies Office [dataset], 2023. https://www.usgs.gov/3d-elevation-program.

Wells, D. and Coppersmith, K. New empirical relationships among magnitude, rupture length, rupture width, rupture area, and surface displacement. *Bulletin of the Seismological Society of America*, 84(4):974–1002, 1994. doi: 10.1785/BSSA0840040974.

Wesnousky, S. Active faulting in the Walker Lane. *Tectonics*, 24: TC3009, 2005. doi: 10.1029/2004TC001645.

Wesnousky, S., Bormann, J., Kreemer, C., Hammond, W., and Brune, J. Neotectonics, Geodesy, Seismic Hazard in the northern Walker Lane of Western North America: Thirty kilometers of crustal shear and no strike-slip? *Earth and Planetary Science Letters*, 329-330:133–140, 2012. doi: 10.1016/j.epsl.2012.02.018.

Yürür, T., Köse, O., Demirbağ, H., Özkaymak, Ç., and Selçuk, L. Could the coseismic fractures of a lake ice reflect the earthquake mechanism?:(Afyon earthquakes of 2 March 2002, Central Anatolia, Turkey). *Geodinamica Acta*, 16(2-6):83–87, 2003. doi: 10.1016/S0985-3111(03)00003-2.

Zuckerman, M., Amos, C., Madugo, C., Elliott, A., Kottke, A., Goulet, C., Meng, X., and Caplan-Auerbach, J. Jumping rocks as an indicator of ground motion during the 4 July 2019 M6.4 Ridgecrest earthquake. *Geological Society of America Abstracts*, 52(6), 2020. doi: 10.1130/abs/2020AM-356342.